Nanoscale

Accepted Manuscript

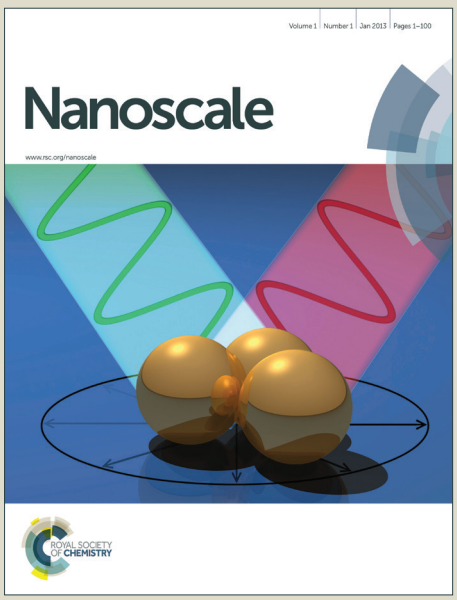

ROYAL SOCIETY OF CHEMISTRY

www.rsc.org/nanoscale

Nanoscale

RSCPublishing

ARTICLE

Simple Fabrication of Flexible Electrode with High Metal-Oxide Content: Electrospun Reduced Tungsten Oxide/Carbon Nanofibers for Lithium Ion Battery Applications

Cite this: DOI: 10.1039/x0xx00000x

Received 00th January 2012,
Accepted 00th January 2012

DOI: 10.1039/x0xx00000x

www.rsc.org/

Jaehyuk Lee,[†,a] Changshin Jo,[†,a] Bangrock Park,[b] Woonbong Hwang,[b] Hyung Ik Lee,[c] Songhun Yoon,[d] Jinwoo Lee*[a]

A one-step and mass-production synthetic route for the flexible reduced tungsten oxide/carbon composite nanofiber (WO_x-C-NF) film is prepared *via* electrospinning technique. A WO_x-C-NF film exhibits unprecedented high content of metal-oxides (~ 80 wt%) and good flexibility (tensile strength of the specimen was 6.13 Mpa) without the use of flexible support materials like CNT or graphene. The WO_x-C-NF film is directly used as an anode in a lithium ion battery (LIB). Compared with previously reported tungsten oxide electrodes, the WO_x-C-NF film exhibits highly reversible capacity (481 mA h $g^{-1}_{\text{total electrode}}$), stable cycle, and improved rate performance, without use of additive carbon, polymeric binder and current collector. Moreover, control electrodes fabricated by conventional processes support the positive effects of both freestanding electrode and metal-oxide embedded carbon 1-D nanofiber structure.

1. Introduction

Flexible energy-storage systems, such as batteries and supercapacitors, have been actively studied for the commercialization of flexible devices, including wearable electronics, electronic paper, roll-up displays, etc.[1, 2] To achieve this, a recent study concentrated on the development of flexible and free-standing electrode films with high chemical and mechanical stability. An efficient synthetic method could simplify the existing complicated electrode production processes, in which conventional powder-type active materials are used. For example, free-standing electrodes do not require binders, carbon additives and metal current collectors. The binder, used to provide close contact between the active materials, the additive carbon and current collector, has its own demerits: i) an electrochemically inactive nature, and ii) a thermal stability problem.[3-6] In addition, the current collector accounts for a substantial portion of the electrode's mass. Usually, 20 μm thick copper substrate that is commonly used in a battery anode, has and areal density of ~15 mg cm^{-2}. Therefore, the use of a binder and current collector results in a great decline in the gravimetric/volumetric power and energy density. Moreover, the conventional electrode production process requires multiple-steps, including slurry production, current-collector coating, drying, and electrode configuration.

Recently, in order to fabricate flexible and free-standing electrodes, various approaches have been developed by many researchers using "flexible materials" such as carbon nanotube (CNT) films, graphene films, porous metal substrates, etc.[7-16] Among these, graphene and CNTs have been employed to construct flexible electrodes in many reported studies. Because of their mechanical flexibility and high electron mobility, both graphene and CNTs have been widely used as flexible supports for transition-metal-oxide loading. Recently, many papers have reported the preparation of flexible metal-oxide/graphene (or CNT) composite films by using filtration or sonication methods.[8-11, 17] These flexible films have been directly used as electrodes in lithium ion batteries (LIBs) or supercapacitors and exhibited reasonable cycle and rate performances.

However, some fundamental limitations are still present. In the case of a graphene electrode, the metal oxide loading content is limited to 50 ~ 60 wt %.[18-21] When the metal loading increases, the film becomes brittle in most cases. In addition, chemically modified graphene, which is composed of several carbon layers, could disturb the diffusion of active ions (Li^+ in LIB case) into the metal-oxide particles.[22, 23] On the other hand, in a case where CNTs are used as a conducting support, it is difficult to disperse hydrophilic active particles on the surfaces of the CNTs because of the hydrophobic nature of these

surfaces. In most cases, the active particles are physically trapped in pores between CNT fibers. Therefore, in order to maximize the electrochemical performance of metal-oxide/CNT nanocomposite, additional processes, are required, such as the introduction of functionalities on CNT surface or addition of surfactant.[24, 25] Moreover, because the homogeneous mixing of the metal-oxide and carbon materials is not guaranteed with a physical mixing approach, the aggregation problem still exists in conversion-based materials. Based on these basic problems, a new approach for flexible film electrodes is urgently needed to realize the mass production of flexible energy storage systems.

Among the various candidates, an electrospinning technique could be a solution to the above-mentioned problems. Electrospinning is a versatile method for the low-cost mass production of nanofibers with diameters ranging from 10 to 1000 nm.[26, 27] When a voltage is applied, an electric force is generated between a polymeric solution in a syringe tip and a substrate, resulting in a jet of the polymeric solution. The length and diameter of the electrospun fiber are easily controlled by adjusting the voltage, concentration and viscosity of the polymeric solution, and the distance between the substrate and the tip. However, it has been difficult to construct a free-standing and flexible inorganic (metal-oxide) film despite the easy fabrication of metal precursor-polymer as-spun fibers. This was because the size of the nanocrystals continues to grow during the calcination process, resulting in a severe deformation of the nanofiber structures.[28-31]

Recently, some free-standing and flexible electrodes have been fabricated through electrospinning approach for applications to energy storage devices.[32, 33] However, there are still limitations to be overcome, such as the multiple fabrication steps (an active material was coated after the fabrication of a carbon nanofiber film using electrospinning[34]) and low metal-oxide loading (10 ~ 20 wt%). A higher metal-oxide content would be favorable for the performance of a real cell. (i) In real battery applications, the volumetric energy/power performance is the most important characteristic. However, carbon-based electrodes exhibit a lower electrode density than metal-oxide-based electrodes. (ii) Carbon electrodes show a low coulombic efficiency of approximately 30~60 %, which produces a considerable Li ion loss in the first cycles.[35, 36] In this sense, it is necessary to develop free-standing and flexible metal-oxide-based films with high metal-oxide loading through a simple electrospinning process.

Tungsten oxides, which are rarely studied for anodes, are attractive materials for anodes because of their multiple oxidation states, low price and high intrinsic density.[37-39] Recently, a few groups have synthesized nanostructured tungsten oxides using various approaches such as a hydrothermal method and spray pyrolysis and have applied them as anode materials in LIBs.[40-43] In our previous study, we synthesized ordered mesoporous reduced tungsten oxide (m-WO_{3-x}) and applied it as an LIB anode material.[44] The partial reduction of the tungsten oxide resulted in an enhanced electrical conductivity due to the intervalence charge transfer between W^{5+} and W^{6+}.[45] This reduced-tungsten-oxide anode exhibited a higher capacity and faster rate performance than other nanostructured tungsten oxides because of the positive effects of the ordered mesoporous structure and enhanced electrical conductivity. Moreover, the reduced tungsten oxides (m-WO_{3-x}) were also successfully applied in various energy related devices including fuel cells, supercapacitors, and dye-sensitized solar cells.[46-50]

In this study, we synthesized electrospun free-standing and flexible tungsten oxide/carbon nanofibers (denoted as WO_x-C-NF) using ammonium-meta-tungstate (AMT) and polyvinylpyrrolidone (PVP) as the tungsten and carbon precursors, respectively. The selection of the precursors and optimization of the synthetic condition resulted in the successful fabrication of a flexible film with a high mass-loading of metal oxide (~80 wt% tungsten oxide). The fabricated WO_x-C-NF film was directly used as an LIB anode without further processing, meaning no current collectors, carbon additive, and binders were needed to fabricate the electrodes. Compared with other tungsten oxide anode studies, our WO_x-C-NF film electrode exhibited a high reversible capacity (481 mA h g^{-1}), coulombic efficiency (74.5 %), and good rate and cycle performances. Because we achieved a high loading of tungsten oxide which has a high intrinsic density, the coulombic efficiency was higher than that in carbon rich free-standing electrodes, and a large amount of electrochemically active materials could be packed into a limited space. Because of the versatility of the electrospinning technique, this process will be applicable to the mass production of electrode films with a low-cost in a short time.

2. Experimental

Preparation of WO_x-C-NF: The electrospun WO_x-C-NF were fabricated using a polymer and tungsten precursor composite solution. First, 0.8 g of amonium-meta-tungstate hydrate ($(NH_4)6H_2W_{12}O_{40}•xH_2O$, Aldrich, 99.99 %) and 0.58 g of polyvinylpyrrolidone (PVP, MW: 1,300,000, Aldrich) were separately dissolved in 2 ml and 6 ml of N, N-dimethylformamide (DMF, Macron chemicals) solution. The two solutions were stirred for 10 h and then homogeneously mixed together. The prepared precursor solution was transferred to a 10 ml plastic syringe. The solution was supplied by syringe pump (KD Scientific, KDS 100). The flow rate of the precursor solution was 0.12 ml h^{-1}, respectively. A single nozzle tip (plastic nozzle tip 21G 1/4, Nanonc. CO.) was used in the electrospinning process. The distance between the nozzle tip and the substrate was 20 cm. A high electrical potential of 11.5 kV was applied to the precursor solution using a power supply. Finally, the as-spun WO_x-C-NF were collected on the substrate. To obtain the WO_x-C-NF, the as spun fibers were heat treated at 700 °C for 2h in a nitrogen atmosphere.

Material characterization: The morphologies of the materials were analyzed using a scanning electron microscope (SEM; JSM-840A, JEOL) and a transmission electron microscope (TEM; JEM-2010, JEOL). X-ray diffraction (XRD)

measurements were taken using a Rigaku D/Max-3C diffractometer equipped with a rotating anode and Cu Kα radiation (λ = 0.15418 nm). Electron energy loss spectroscopy (EELS) images of the WO_x-C NF were obtained using a JEM-2200FS (JEOL) instrument. Thermogravimetric and differential thermal analyses (TGA/DTA) were performed on an SII EXSTAR 6000 thermal analyzer at a heating rate of 10 °C min^{-1}. Raman spectrum analysis was performed on a LabRam ARAMIS (460 mm focal length monochromator with air cooled (-70 °C) CCD multichannel detector). The flexible properties of the WO_x-C-NFs film was measured by using MTS Nano Universal Testing System (Nano UTM).

Electrochemical characterization: An electrochemical test was conducted using a Coin-type two-electrode cell (CR2032). The electrospun (WO_x-C-NF) were directly used as an electrode after cutting the film into a round shape with a diameter of 14 mm. For the control experiment, WO_x-C-Nano and WO_x-Nano slurries were prepared by mixing the electrode materials with binder (polyvinylidene difluoride) and additive carbon (Super P) (mass ratio of 8 : 1 : 1) in N-methyl-2-pyrrolidone (NMP). After mixing, the slurries were coated on a Cu foil. The electrodes were dried at 110 °C in a vacuum oven for 12 h. Finally, the electrodes were punched into 14 mm diameter circles. The coin cells were assembled using prepared electrodes with lithium metal foil, polyethylene separator, and electrolyte (1.0 M $LiPF_6$ in ethylene carbonate/dimethyl carbonate, 1 : 1 volume ratio, Panaxetec Co., KOREA) in a glove box. A galvanostatic charge/discharge test was performed using a WBCS-3000 battery cycler (Xeno Co.) with various current densities (0.05 to 5 A g^{-1}) in a potential range of 3.0 to 0.01 V (vs. Li/Li^+). Cyclic voltammetry (CV) and electrochemical impedance spectroscopy (EIS) tests were conducted using a Reference 600 potentiostat (Gamry Instruments, USA). The voltage range for the CV test was 3 to 0.01 V with a scan rate of 0.15 mV s^{-1}. The EIS test was conducted under different voltage conditions (OCV of pure cells and 0.01 V after 5 cycles) in a frequency range of 10^5 to 0.01 Hz under an AC stimulus with a 5 mV amplitude. For ex-situ SEM study, the cells were disassembled in the glove box and the electrodes were washed with anhydrous dimethyl carbonate (99%, Aldrich). After drying, the electrodes were attached to the carbon tape for sample fixation.

3. Results and discussion

3.1. Synthesis of WO_x-C-NF via electrospinning

The synthetic procedure for the flexible WO_x-C-NF film is summarized in Scheme 1. A polymeric solution was prepared by the homogenous mixing of AMT, PVP, and N, N-dimethylformamide. Subsequently, this polymeric solution was introduced into the nozzle by syringe pumps. When a voltage was applied, the as-spun nanofiber web was formed by a jet of the polymeric solution. Finally, the WO_x-C-NF film was obtained by heat-treatment at 700 °C under a nitrogen atmosphere. Although the film size shrank upon heat-treatment, the free-standing and flexible characteristics were maintained after heat treatment. The morphology of the WO_x-C-NF was studied using scanning electron microscopy (SEM).

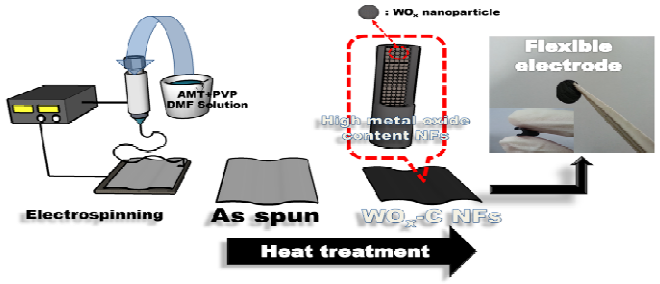

Scheme 1. Schematic illustration of electrospinning process for synthesis of flexible WO_x-C-NF electrode.

Figure 1A shows the as-spun film which consisted of nanoscale fibers with an average diameter of 190 ± 60 nm with a high aspect ratio. The as-spun WO_x-C-NF film had a common flexible property like a fabric (inset of Figure 1A). After heat treatment at 700 °C under a nitrogen atmosphere, the size of the free-standing film and the diameter of the nanofibers were reduced by thermal shrinkage from the decomposition of the inorganic precursors and polymer. (Figure 1B and supporting information, S1) The average diameter of the WO_x-C-NF was 135 ± 85 nm.

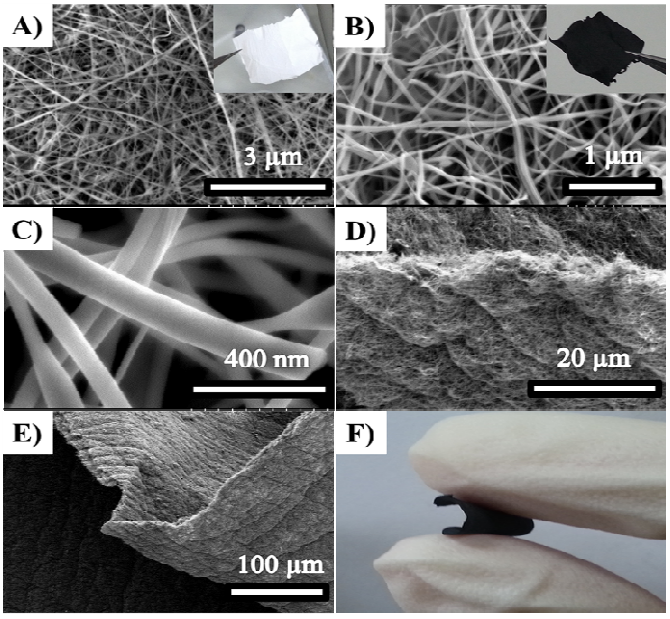

Figure 1. SEM images of A) as-spun nanofibers, B) nanofibers after heat-treatment at 700 °C, and C) WO_x-C-NF at high magnification. D) and E) SEM images of folded region of WO_x-C-NF. F) Digital photograph of bent WO_x-C-NF film.

Interestingly, as seen in Figure 1C, the WO_x-C-NF show a smooth surface without any bead formation or particle aggregation on the surface of the nanofibers, indicating that small WO_x nanoparticles could be well embedded and

distributed inside the nanofiber. In general, after the calcination process, the electrospun metal-oxide nanofibers revealed a rough surface or sintered particle morphology like a string of pearls.[28-31, 51] Consequently, the as-electrospun film could not sustain its original free-standing properties after high-temperature heat-treatment. Figure 1F shows a digital photograph of the bent WO_x-C-NF film. The SEM image of the folded region of the WO_x-C-NF film also reveals that its bent part not collapsed (Figure 1E), and the unbroken long nanofibers are continuously tangled with each other in a large range for the entire web (Figure 1D). These results support the conclusion that the WO_x-C-NF film maintains flexible properties even after heat treatment at a high temperature.

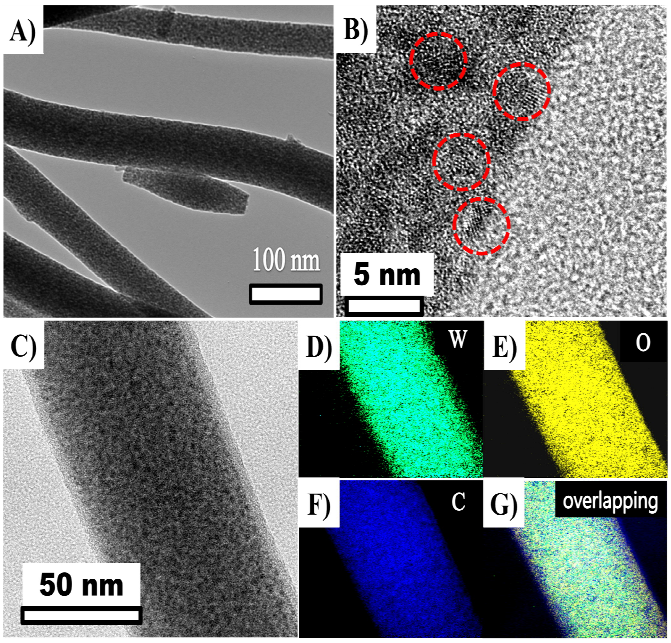

Figure 2. A) TEM image of WO_x-C-NF. B) HR-TEM image of WO_x-C-NF. C) HR-TEM image of the WO_x-C-NF and corresponding electron energy loss spectroscopy (EELS) mapping images of the D) W, E) O, F) C, and G overlapping of the W, O, and C contents.

To investigate the morphology of the WO_x-C-NF in more detail, a transmission electron microscope (TEM) study was performed (Figure 2). As confirmed in the SEM studies, the smooth surfaces of the WO_x-C-NF are observed, and there are no exposed large and sintered inorganic particles, as shown in Figure 2A. A high-resolution TEM (HR-TEM) image showed that the small WO_x nanoparticles (less than 3 nm) were uniformly dispersed inside the amorphous carbon matrix generated from the carbonization of PVP (Figure 2B and C). Figure S2 shows the XRD patterns of WO_x-C-NF, where WO_x corresponds to a reduced form of the $WO_{2.83}$ phase (JCPDS No.036-0103, Figure S3). Reduced tungsten oxides are better electrode materials than WO_3 because of their enhanced electrical conductivity and capacities.[44] The mean crystallite size of WO_x was estimated to be 1.5 nm by the Scherrer equation using the width at half-maximum of the main peak corresponding to the (010) reflection.

This amorphous carbon matrix could prevent the growth of WO_x particles during heat treatment.[33, 52] The uniform distribution of the small nano-sized WO_x crystallites inside the carbon matrix was probably the main reason for the flexible property of the WO_x-C-NF even with a high loading of tungsten oxides. To prove that the uniform small particles were crucial to the flexible property, the as-spun of WO_x-C-NF film was heat-treated at higher temperature, 900 °C, (Figure S4). The particle size was significantly increased and the flexible property was lost.

Electron energy loss spectroscopy (EELS) mapping images of the W, O, and C contents of the WO_x-C-NF are presented in Figure 2D-G. The HR-TEM images (Figure 2B and C), along with the corresponding EELS mapping images, again confirmed that the tungsten oxide particles were embedded inside the amorphous carbon. It should be noted that the overlapping image, as shown in Figure 2G, reveals that thin C-element layers (blue color) are formed on the outer surface of the nanofiber. This carbon layer could have been generated from the decomposition of polymer content during the heat treatment.[53-55] When the polymer content was decomposed with increasing temperature, gases, such as carbon monoxide, could force out relatively light organic species out to the nanofibers, and the organic-species-rich region on the shell of the nanofiber was converted to a thin carbon shell. When WO_x-C-NF is used as an anode, this carbon layer can provide WO_x particles with a carhigh chemical stability and a protecting layer the during charge/discharge reaction.[54-56]

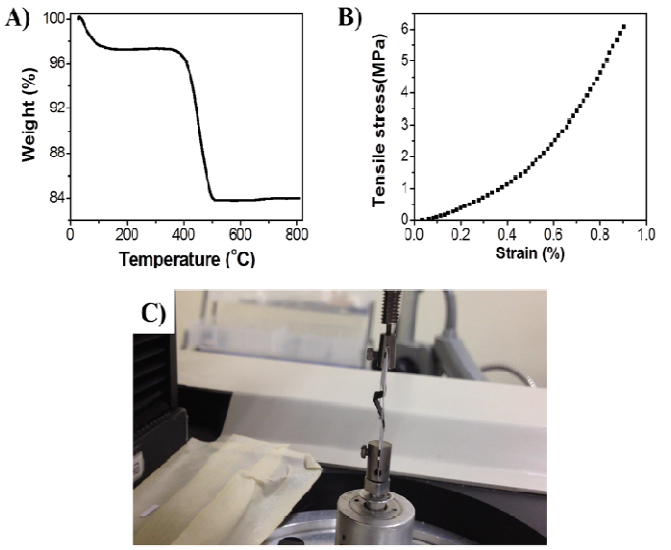

Figure 3. A) TGA data of WO_x-C-NF. B) Tensile test data of the WO_x-C-NF Web. C) A digital photograph of the WO_x-C NF in an MTS Nano Universal Testing System.

To confirm the metal-oxide and carbon contents in the synthesized WO_x-C-NF, a thermogravimetric analysis (TGA) was performed under an air atmosphere. As shown in Figure 3A, the weight of the WO_x-C-NF is reduced between 400 °C and 550 °C by the oxidation of amorphous carbon. Surprisingly, although the flexibiliy is given to WO_x-C-NF, its

weight loss was only 17 wt% which was similar to the carbon content measured from the CHN elemental analysis (15 wt%).

In order to study the bending property of the WO_x-C-NF film, tensile tests were performed on the film (Figure 3B). The gauge length of the specimen was fixed at 10 mm. The specimen was mounted on a paper jig and set onto an MTS Nano Universal Testing System (Nano UTM), as shown in Figure 3C. The sides of the paper jig were cut off and the specimen was stretched at a constant strain rate of 0.027 mm/s. The data for a specimen that fractured within the gauge length were used for the mechanical properties. The tensile strength of the specimen was 6.13 Mpa, and maximum strain was 0.9%. Despite the high metal-oxide loading (83 wt%), the WO_x-C-NF film showed a high strength, which supported its free-standing property, as confirmed by a microscope analysis.

Based on the above characterizations, we can conclude that the flexibility of WO_x-C-NF is produced by their unique fiber structure: very small particles (~ 2 nm) embedded in an amorphous carbon matrix. The key factor for this indestructible nanofiber is the proper selection of the AMT precursor for the tungsten oxide. The AMT precursor is decomposed into tungsten blue oxide (reduced form) in an inert gas.[57-59] This indicates that small WO_x crystals are formed inside the carbon without any oxygen precursor. Moreover, it seems that the functional groups in PVP such as nitrogen and oxygen interact with AMT inside the nanofiber, which is responsible for the formation of small-sized nanoparticles. Although PVP is not a common carbon source because of its low conversion yield (less than 10 wt %),[60-62] in this work, 14% of the PVP was converted to conducting amorphous carbon, producing 17 wt% of the carbon in the WO_x-C-NF. Figure S5 shows the Raman spectrum of the WO_x-C-NFs. Two bands, around 1350 cm^{-1} and 1590 cm^{-1}, represent the disordered carbon (D-band) and graphitic carbon (G-band), respectively.[63] Recently, Wang et al. reported that PVP as-spun nanofiber could be converted into carbon nanofiber by appropriate heat treatment processes, including stabilization, pre-oxidation, and carbonization.[64] Similarly, the interaction between AMT and PVP probably aids in the stabilization and carbonization of the PVP during the heat treatment. However, further study is required to clarify the interaction between the two precursors.

3.2. Electrochemical Characteristics of WO_x-C-NF

In order to test the applicability of WO_x-C-NF to current-collector-free and free-standing battery electrodes that do not require binder and carbon additives, CR 2032 coin-type cells were assembled using the WO_x-C-NF film as a working electrode and Li metal as counter and reference electrode. The WO_x-C-NF film was cut into a disk-shape with a diameter of 14 mm (Scheme 1) and used directly as electrode. In order to demonstrate the high performance of the WO_x-C-NF electrode, two control bulk powder samples were prepared: (1) WO_x-C-Nano by heat treatment of an AMT/PVP polymeric solution (without the electrospinning process) and (2) carbon-free WO_x-Nano by the thermal decomposition of AMT under a nitrogen atmosphere (700 °C). To investigate the phases and morphologies of these comparison samples, XRD and TEM analyses were performed, as shown Figure S6. The XRD pattern of the WO_x-C-Nano was confirmed to be the $WO_{2.83}$ phase (JCPDS No. 036-0103) and the mean crystallite size was 6.6 nm, as calculated using the Debye-Scherrer equation. The WO_x-Nano sample corresponded to the WO_3 phase (JCPDS No. 98-001-5905), and the particle size was 40 nm (Figure S6A and C). Figure S6B and D shows the structures of the control samples, as investigated by TEM. The carbon content of WO_x-C-Nano sample was confirmed by elemental analysis. The carbon content of WO_x-C-Nano was 17 wt%, similar to that in the WO_x-C-NF. WO_x-C-Nano and WO_x-Nano electrodes were produced by mixing the active materials with conducting carbon (Super P) and binder (polyvinylidene difluoride) in a mass ratio of 8 : 1 : 1. The mass of a WO_x-C-NF electrode was 2 ~ 3 mg and the total loadings of the WO_x-C-Nano and WO_x-Nano electrodes were 2.5 mg and 3.3 mg on a copper current collector with a diameter of 14 mm, respectively.

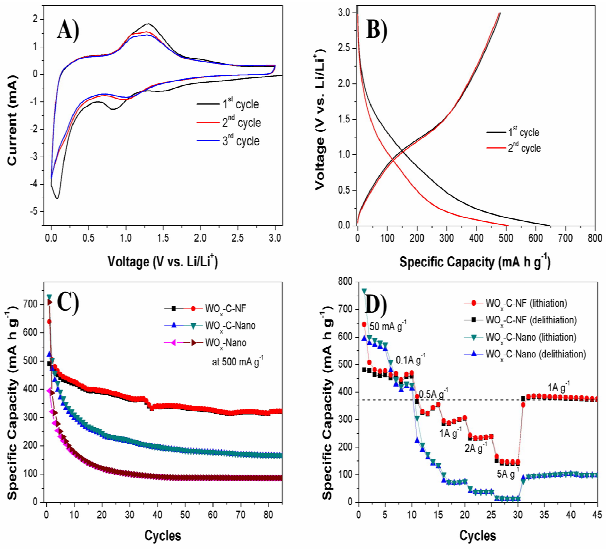

Figure 4. Electrochemical characterization of WO_x-C-NF electrode. (A) Cyclic voltammetry at a scan rate of 0.15 mV s^{-1} and (B) galvanostatic charge/discharge profiles measured at a 50 mA g^{-1} current density in the potential range of 0.01-3.0 V vs. Li/Li^+. (C) Capacity retention profiles of WO_x-C-NF, WO_x-C-Nano, and WO_x-Nano electrodes. The charge/discharge rate was fixed at 500 mA g^{-1}. (D) Capacity changes of WO_x-C-NF and WO_x-C-Nano electrodes under different current density conditions (0.05-5 A g^{-1}).

To investigate the lithiation and delithiation of WO_x-C-NF electrode, a cyclic voltammetry (CV) analysis was conducted at a scan rate of 0.15 mV s^{-1} (Figure 4A). The electrode exhibited several cathodic and anodic peaks, corresponding to the multiple reduction and oxidation reactions of WO_x. In the first cathodic process, the peak at 1.5 V was attributed to the irreversible process, and a portion of this reaction was involved in the Li^+ intercalation into the WO_x crystals.[65-67] The peak near 0.8 V was related to the initiation of the WO_x reduction and the formation of a solid electrolyte interface (SEI) layer. In previous studies, most tungsten-oxide materials exhibited an intense peak at the first cycle, indicating a large amount of SEI formation on the tungsten-oxide surface or the decomposition

of WO_x crystal by conversion reaction.[43, 44, 65-67] As shown in Figure S7B, the WO_x-Nano electrode also has a strong cathodic peak centered at 0.75 V. However, the free-standing WO_x-C-NF electrode exhibited a weak cathodic peak at this potential. Similarly, the WO_x-C-Nano electrode also shows a weak cathodic peak (Figure S7A). This indicates that the amorphous carbon enveloping the WO_x nanocrystal could suppress the SEI formation reaction or a severe structural change in the WO_x crystal.[68-72] The following cathodic peaks below 0.3 V are the results of a further reduction reaction, W^{5+} or W^{6+} into a low oxidation state (W^0) following the equation:

$$WO_x + 2xLi^+ + 2xe^- \leftrightarrow W + xLi_2O \qquad (1)$$

The conversion reaction produces a W metal and Li_2O amorphous mixture during the first lithiation process.[44, 67] Although the broad anodic peak centered at 1.3 V decreased during the initial cycles, both the cathodic and anodic processes were reversible in the WO_x-C-NF electrode.

Figure 4B shows the galvanostatic charge/discharge curves of WO_x-C-NF electrode (2 mg) with a current density of 50 mA g^{-1}. The WO_x-C-NF electrode exhibited initial discharge (lithiation) and charge (delithiation) capacities of 646 mA h g^{-1}_{total} and 481 mA h g^{-1}_{total}, respectively. The WO_x-C-Nano electrode, on the other hand, showed first discharge and charge capacities of 770 mA h $g^{-1}_{WOx\text{-}C}$ and 594 mA h $g^{-1}_{WOx\text{-}C}$ (Figure S7C). Considering the mass of the copper film, binder and conducting carbon, the total reversible capacity of WO_x-C-Nano electrode is much lower, $C_{electrode}$: ~44 mA h g^{-1} total (the total mass of the WO_x-C-Nano electrode is 27.0 mg). This indicates that the electrospun free-standing electrode could increase the gravimetric energy and power densities of the LIBs as a result of its lightweight and free-standing features. The initial coulombic efficiency of WO_x-C-NF electrode (74.5 %) was comparable to that of the WO_x-C-Nano electrode (77.1 %) and higher than that of other nanostructured tungsten oxide electrodes (45~70 %).[39-44] On the other hand, the pure WO_x-Nano electrode showed a lower initial coulombic efficiency of 63.1 % compared to the WO_x/carbon composite electrodes (Figure S7D, 773 and 488 mA h g^{-1}_{WOx} for the lithiation and delithiation capacities, respectively).

Figure 4C shows the cycle performances of WO_x-C-NF, WO_x-C-Nano and WO_x-Nano electrodes. Using 3 mg WO_x-C-NF film, the cell was charged and discharged with a current density of 500 mA g^{-1}. In previous studies, tungsten-oxide anodes have shown a noticeable capacity degradation during the initial few cycles.[39, 41, 42] In our study, the WO_x-C-Nano and WO_x-Nano electrodes also exhibited capacity declines during the initial 10 cycles. However, the WO_x-C-NF film electrode exhibited a more stable cycle performance. The reversible capacity of WO_x-C-NF electrode after 85 cycles was 321 mA h g^{-1} (65.6% retention). However, only 164 mA h g^{-1} (31.4%) and 85 mA h g^{-1} (21.6%) were maintained in the WO_x-C-Nano and WO_x-Nano electrodes. In general, the destruction of the electrode integrity causes this decrease in capacity in conventional tungsten-oxide cell configurations that consist of a carbon additive, binder, and current collector. From the cycle data, we conclude that the enhanced cycle performance of WO_x-C-NF electrode can be attributed to both the carbon composite and 1-D nanofiber structure effects. The amorphous carbon shell provides a layer of protection against the SEI formation and mitigates the structural degradation of WO_x particles during cycles. Moreover, in WO_x-C-NF, the ultra-fine WO_x nanoparticles (< 3 nm) are trapped inside the 1-D carbon nanofiber with a homogenous mixing, resulting in good electrical contact and improved structural stability.[68-72] Figure S8A shows the coulombic efficiency (CE) values of three tungsten oxide cells. The plots correspond to the cycle data in Figure 4C. At first cycle, their CE values were 76.6, 71.8, and 55.7% for WO_x-C-NF, WO_x-C-Nano and WO_x-Nano electrodes, respectively. From second cycle, all electrodes showed a rapid increase in CE values, especially in WO_x-C-NF electrode. The CE values in WOx-C-NF cell were over 98% from 8th cycle, while more than 22 cycles were required to reach that value in other electrode cases. The results indicate that the WO_x-C-NF has the best reversible charge-discharge performance.

The rate performance of WO_x-C-NF electrode (2 mg) was investigated by charging/discharging the cells with current density range of 0.05~5 A g^{-1} (Figure 4D). In the early cycles, the WO_x-C-NF film electrode presented stable charge/discharge capacities, whereas the capacities of the WO_x-C-Nano electrode dropped under a slow charging rate condition of 50~100 mA g^{-1}. At a current density of 50 mA g^{-1}, the delithiation capacities of the WO_x-C-NF and WO_x-C-Nano electrodes were 481 mA h g^{-1} and 594 mA h g^{-1}, respectively. However, as the current densities increased, the capacity fading was severe in the WO_x-C-Nano electrode, 39 (7 %) and 12 (2 %) mA h g^{-1} at 2 and 5 A g^{-1}, respectively. On the other hand, the WO_x-C-NF electrode had a better rate performance of 232 (48 %) and 150 (31 %) mA h g^{-1} under the same current conditions. It should be noted that WO_x-C-NF electrode showed a better rate performance even without the use of any carbon additive and metal current collector (Conducting carbon and binder were used in the case of WO_x-C-Nano and WO_x-Nano electrodes). When the current density was reduced to 1 A g^{-1}, the charge capacity value of the WO_x-C-NF electrode was 375 mA h g^{-1}, which was slightly higher than the theoretical capacity of graphite (372 mA h g^{-1}). The reversible capacities of both electrodes at 31st cycle were higher than the capacity values at the 16th cycle, even at the same current density of 1 A g^{-1}. The capacity increase during the cycles is not surprising for the conversion-based metal-oxide anodes.[73-76] Based on the data, we can conclude that our electrospun WO_x-C-NF electrode shows overwhelming cycle and rate performances, compared with those of the WO_x-C-Nano particles and tungsten oxides in other studies.[39-42, 44, 67] In addition, the *ex-situ* SEM images of WO_x-C-NF after 50 cycles exhibit well-preserved 1-D nanofiber structure with a small portion of aggregated particles on the nanofibers (Figure S9). The SEM images represent that the WO_x nanoparticles are somehow aggregated during the conversion reaction (equation 1), but unique 1-D structure of WO_x-C-NF is well-maintained during the 50 cycles.

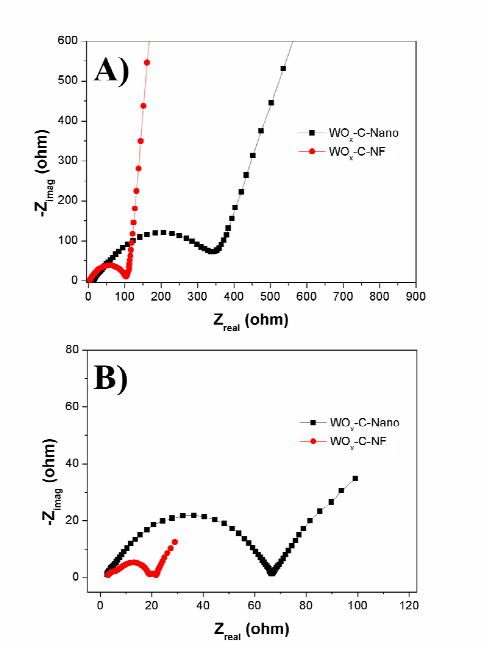

Figure 5. Nyquist plots of WO_x-C-NF and WO_x-C-Nano electrodes from electrochemical impedance spectroscopy, measured at (A) initial state (OCV) and (B) fully lithiated state after 5 charge / discharge cycles

To compare the resistance properties, an electrochemical impedance spectroscopy (EIS) analysis was conducted in the frequency range of 10^5 to 10^{-2} Hz. Figure 5A and B show the Nyquist plots of the WO_x-C-NF and WO_x-C-Nano electrodes under pure (at OCV) and fully lithiated (after 5 charge/discharge cycles) conditions, respectively. Both electrodes showed characteristic graphs, composed of a semicircle and sloped line. Typically, the semicircle in the high frequency region represents the charge-transfer resistance between the electrode and the electrolyte. The sloped line in the low frequency region is related to the Warburg diffusional process for Li ions into the electrode. In a rough comparison, it is easily confirmed that the WO_x-C-NF electrode exhibits much smaller impedance values than those of the WO_x-C-Nano electrode under different voltage conditions. This indicates that both the charge-transfer and ion-diffusion processes are quite effective in the electrospun electrode. This resistance property occurs because the carbon framework provides an electron path to the WO_x nanocrystals, and 1-D nanofiber structure facilitates Li ion diffusion to the metal oxide.

4. Conclusions

In conclusion, despite the fact that the film has 83 wt% metal oxide, we developed a free-standing and flexible WO_x-C-NF film using a one-step electrospinning process. The film was used directly as a free-standing anode for LIBs and exhibited a higher stability and rate performance than normal WO_x-C-Nano and WO_x-Nano electrodes. This result indicates that the "one-step electrospinning technique" is more economical than the conventional electrode fabrication because no polymeric binder, additive carbon, and current collector are employed to fabricate free-standing electrodes for LIBs. This approach can be extended to other high capacity metal-oxide materials to fabricate high performance flexible batteries.

Acknowledgements

This work was supported by Defense Acquisition Program Administration and Agency for Defense Development under the contract UD110090GD. This work was further supported by the Global Frontier R&D Program on Center for Multiscale Energy System funded by the National Research Foundation under the Ministry of Education, Science and Technology, Korea. This research was also supported by a National Research Foundation of korea grant funded by the Korean Government (2012R1A2A2A01002879). This work was further supported by a grant of the Korea Health 21 R&D Project, Ministry of Health & Welfare (A121631). This research was a part of the project titled 'Technology Development of Marine Industrial Biomaterials', funded by the Ministry of Oceans and Fisheries, Korea. This research was supported by Basic Science Research Program through the National Research Foundation of Korea (NRF) funded by the Ministriy of Science, ICT and Future Planning (NRF-2013R1A1A2074550)

Notes and references

[a] Department of Chemical Engineering, Pohang University of Science and Technology (POSTECH), Pohang, 790-784, Republic of Korea. E-mail: Jinwoo03@postech.ac.kr
[b] Department of Mechanical Engineering, Pohang University of Science and Technology (POSTECH), Pohang, 790-784, Republic of Korea.
[c] 4-3 Agency for Defense Development, Daejeon, 35-4, Republic of Korea.
[d] Department of Integrative Engineering Chung-Ang University 221, Heukseok-Dong, Dongjak-Gu, Seoul, 156-756, Republic of Korea.

† Electronic Supplementary Information (ESI) available: [details of any supplementary information available should be included here]. See DOI: 10.1039/b000000x/

† These authors contributed equally to this work.

Reference

1. J. M. Tarascon and M. Armand, *Nature*, 2001, **414**, 359-367.
2. H. Nishide and K. Oyaizu, *Science*, 2008, **319**, 737-738.
3. H. Maleki, G. Deng, I. Kerzhner-Haller, A. Anani and J. N. Howard, *J. Electrochem. Soc.*, 2000, **147**, 4470-4475.
4. M. N. Richard and J. R. Dahn, *J. Power Sources*, 1999, **83**, 71-74.
5. L. Fransson, T. Eriksson, K. Edström, T. Gustafsson and J. O. Thomas, *J. Power Sources*, 2001, **101**, 1-9.
6. P. Biensan, B. Simon, J. P. Pérès, A. de Guibert, M. Broussely, J. M. Bodet and F. Perton, *J. Power Sources*, 1999, **81–82**, 906-912.
7. J. Jiang, Y. Li, J. Liu, X. Huang, C. Yuan and X. W. Lou, *Adv. Mater.*, 2012, **24**, 5166-5180.
8. D.-W. Wang, F. Li, J. Zhao, W. Ren, Z.-G. Chen, J. Tan, Z.-S. Wu, I. Gentle, G. Q. Lu and H.-M. Cheng, *ACS Nano*, 2009, **3**, 1745-1752.
9. C. Wang, D. Li, C. O. Too and G. G. Wallace, *Chem. Mater.*, 2009, **21**, 2604-2606.

10. H. Gwon, H.-S. Kim, K. U. Lee, D.-H. Seo, Y. C. Park, Y.-S. Lee, B. T. Ahn and K. Kang, *Energy Environ. Sci.*, 2011, **4**, 1277-1283.
11. J.-Z. Wang, C. Zhong, S.-L. Chou and H.-K. Liu, *Electrochem. Commun.*, 2010, **12**, 1467-1470.
12. J. Chen, Y. Liu, A. I. Minett, C. Lynam, J. Wang and G. G. Wallace, *Chem. Mater.*, 2007, **19**, 3595-3597.
13. S. W. Lee, J. Kim, S. Chen, P. T. Hammond and Y. Shao-Horn, *ACS Nano*, 2010, **4**, 3889-3896.
14. J. Chen, A. I. Minett, Y. Liu, C. Lynam, P. Sherrell, C. Wang and G. G. Wallace, *Adv. Mater.*, 2008, **20**, 566-570.
15. J.-Y. Choi, D. J. Lee, Y. M. Lee, Y.-G. Lee, K. M. Kim, J.-K. Park and K. Y. Cho, *Adv. Funct. Mater.*, 2013, **23**, 2108-2114.
16. X. Lang, A. Hirata, T. Fujita and M. Chen, *Nat. Nanotechnol.*, 2011, **6**, 232-236.
17. S. Luo, K. Wang, J. Wang, K. Jiang, Q. Li and S. Fan, *Adv. Mater.*, 2012, **24**, 2294-2298.
18. D. Wang, R. Kou, D. Choi, Z. Yang, Z. Nie, J. Li, L. V. Saraf, D. Hu, J. Zhang, G. L. Graff, J. Liu, M. A. Pope and I. A. Aksay, *ACS Nano*, 2010, **4**, 1587-1595.
19. J. K. Lee, K. B. Smith, C. M. Hayner and H. H. Kung, *Chem. Commun.*, 2010, **46**, 2025-2027.
20. J. W. Lee, S. Y. Lim, H. M. Jeong, T. H. Hwang, J. K. Kang and J. W. Choi, *Energy Environ. Sci.*, 2012, **5**, 9889-9894.
21. Z. Li, Y. Mi, X. Liu, S. Liu, S. Yang and J. Wang, *J. Mater. Chem.*, 2011, **21**, 14706-14711.
22. H. Kim, Y. Son, C. Park, J. Cho and H. C. Choi, *Angew. Chem.*, 2013, **125**, 6113-6117.
23. F. Yao, F. Güneş, H. Q. Ta, S. M. Lee, S. J. Chae, K. Y. Sheem, C. S. Cojocaru, S. S. Xie and Y. H. Lee, *J. Am. Chem. Soc.*, 2012, **134**, 8646-8654.
24. A. Gomathi, S. R. C. Vivekchand, A. Govindaraj and C. N. R. Rao, *Adv. Mater.*, 2005, **17**, 2757-2761.
25. Y. Liu and L. Gao, *Carbon*, 2005, **43**, 47-52.
26. V. Kalra, S. Mendez, J. H. Lee, H. Nguyen, M. Marquez and Y. L. Joo, *Adv. Mater.*, 2006, **18**, 3299-3303.
27. N. S. Hansen, D. Cho and Y. L. Joo, *Small*, 2012, **8**, 1510-1514.
28. L. Mai, L. Xu, C. Han, X. Xu, Y. Luo, S. Zhao and Y. Zhao, *Nano Lett.*, 2010, **10**, 4750-4755.
29. L. Li, X. Yin, S. Liu, Y. Wang, L. Chen and T. Wang, *Electrochem. Commun.*, 2010, **12**, 1383-1386.
30. A. L. Viet, M. V. Reddy, R. Jose, B. V. R. Chowdari and S. Ramakrishna, *J. Phys. Chem. C*, 2009, **114**, 664-671.
31. C. T. Cherian, J. Sundaramurthy, M. Kalaivani, P. Ragupathy, P. S. Kumar, V. Thavasi, M. V. Reddy, C. H. Sow, S. G. Mhaisalkar, S. Ramakrishna and B. V. R. Chowdari, *J. Mater. Chem.*, 2012, **22**, 12198-12204.
32. B. Zhang, Y. Yu, Z. Huang, Y.-B. He, D. Jang, W.-S. Yoon, Y.-W. Mai, F. Kang and J.-K. Kim, *Energy Environ. Sci.*, 2012, **5**, 9895-9902.
33. F. Zhang, C. Yuan, J. Zhu, J. Wang, X. Zhang and X. W. Lou, *Adv. Funct. Mater.*, 2013, **23**, 3909-3915.
34. S. Liu, Z. Wang, C. Yu, H. B. Wu, G. Wang, Q. Dong, J. Qiu, A. Eychmüller and X. W. Lou, *Adv. Mater.*, 2013, **25**, 3462-3467.
35. H. Zhou, S. Zhu, M. Hibino, I. Honma and M. Ichihara, *Adv. Mater.*, 2003, **15**, 2107-2111.
36. C. Jo, S. An, Y. Kim, J. Shim, S. Yoon and J. Lee, *Phys. Chem. Chem. Phys.*, 2012, **14**, 5695-5704.
37. G. Leftheriotis, S. Papaefthimiou, P. Yianoulis and A. Siokou, *Thin Solid Films*, 2001, **384**, 298-306.
38. A. Siokou, G. Leftheriotis, S. Papaefthimiou and P. Yianoulis, *Surf. Sci.*, 2001, **482–485, Part 1**, 294-299.
39. J. Yin, H. Cao, J. Zhang, M. Qu and Z. Zhou, *Cryst. Growth Des.*, 2013, **13**, 759-769.
40. Y. Qiu, G.-L. Xu, Q. Kuang, S.-G. Sun and S. Yang, *Nano Res.*, 2012, **5**, 826-832.
41. J. Yang, L. Jiao, Q. Zhao, Q. Wang, H. Gao, Q. Huan, W. Zheng, Y. Wang and H. Yuan, *J. Mater. Chem.*, 2012, **22**, 3699-3701.
42. L. Gao, X. Wang, Z. Xie, W. Song, L. Wang, X. Wu, F. Qu, D. Chen and G. Shen, *J. Mater. Chem. A*, 2013, **1**, 7167-7173.
43. C. M. Sim, Y. J. Hong and Y. C. Kang, *ChemSusChem*, 2013, **6**, 1320-1325.
44. S. Yoon, C. Jo, S. Y. Noh, C. W. Lee, J. H. Song and J. Lee, *Phys. Chem. Chem. Phys.*, 2011, **13**, 11060-11066.
45. S. Shi, X. Xue, P. Feng, Y. Liu, H. Zhao and T. Wang, *J. Cryst. Growth*, 2008, **310**, 462-466.
46. E. Kang, S. An, S. Yoon, J. K. Kim and J. Lee, *J. Mater. Chem.*, 2010, **20**, 7416-7421.
47. S. Yoon, E. Kang, J. K. Kim, C. W. Lee and J. Lee, *Chem. Commun.*, 2011, **47**, 1021-1023.
48. C. Jo, I. Hwang, J. Lee, C. W. Lee and S. Yoon, *J. Phys. Chem. C*, 2011, **115**, 11880-11886.
49. I. Jeong, C. Jo, A. Anthonysamy, J.-M. Kim, E. Kang, J. Hwang, E. Ramasamy, S.-W. Rhee, J. K. Kim, K.-S. Ha, K.-W. Jun and J. Lee, *ChemSusChem*, 2013, **6**, 299-307.
50. C. Jo, J. Hwang, H. Song, A. H. Dao, Y.-T. Kim, S. H. Lee, S. W. Hong, S. Yoon and J. Lee, *Adv. Funct. Mater.*, 2013, **23**, 3747-3754.
51. K. Tang, X. Mu, P. A. van Aken, Y. Yu and J. Maier, *Adv. Energy Mater.*, 2013, **3**, 49-53.
52. J. Lee, M. Christopher Orilall, S. C. Warren, M. Kamperman, F. J. DiSalvo and U. Wiesner, *Nat Mater*, 2008, **7**, 222-228.
53. C. Zhu, Y. Yu, L. Gu, K. Weichert and J. Maier, *Angew. Chem. Int. Ed.*, 2011, **50**, 6278-6282.
54. W. Luo, X. Hu, Y. Sun and Y. Huang, *Phys. Chem. Chem. Phys.*, 2011, **13**, 16735-16740.
55. E. Hosono, Y. Wang, N. Kida, M. Enomoto, N. Kojima, M. Okubo, H. Matsuda, Y. Saito, T. Kudo, I. Honma and H. Zhou, *ACS Appl. Mater. Interfaces*, 2009, **2**, 212-218.
56. W. H. Shin, H. M. Jeong, B. G. Kim, J. K. Kang and J. W. Choi, *Nano Lett.*, 2012, **12**, 2283-2288.
57. R. W. Mooney, V. Chiola, C. W. W. Hoffman and C. D. Vanderpool, *J. Electrochem. Soc.*, 1962, **109**, 1179-1182.
58. G. J. French and F. R. Sale, *J. Mater. Sci.*, 1981, **16**, 3427-3436.
59. M. J. G. Fait, H. J. Lunk, M. Feist, M. Schneider, J. N. Dann and T. A. Frisk, *Thermochim. Acta*, 2008, **469**, 12-22.
60. H. Niu, J. Zhang, Z. Xie, X. Wang and T. Lin, *Carbon*, 2011, **49**, 2380-2388.
61. Y. K. Du, P. Yang, Z. G. Mou, N. P. Hua and L. Jiang, *J. Appl. Polym. Sci.*, 2006, **99**, 23-26.
62. W. N. W. Salleh and A. F. Ismail, *AIChE J.*, 2012, **58**, 3167-3175.
63. F. Su, J. Zeng, X. Bao, Y. Yu, J. Y. Lee and X. S. Zhao, *Chem. Mater.*, 2005, **17**, 3960-3967.

64. P. Wang, D. Zhang, F. Ma, Y. Ou, Q. N. Chen, S. Xie and J. Li, *Nanoscale*, 2012, **4**, 7199-7204.
65. A. Yu, N. Kumagai and H. Yashiro, *Solid State Ionics*, 1997, **100**, 267-273.
66. Q. Wang, Z. Wen, Y. Jeong, J. Choi, K. Lee and J. Li, *Nanotechnology*, 2006, **17**, 3116.
67. W.-J. Li and Z.-W. Fu, *Appl. Surf. Sci.*, 2010, **256**, 2447-2452.
68. M. F. Hassan, Z. P. Guo, Z. Chen and H. K. Liu, *J. Power Sources*, 2010, **195**, 2372-2376.
69. N. Sharma, K. M. Shaju, G. V. Subba Rao, B. V. R. Chowdari, Z. L. Dong and T. J. White, *Chem. Mater.*, 2004, **16**, 504-512.
70. W.-M. Zhang, X.-L. Wu, J.-S. Hu, Y.-G. Guo and L.-J. Wan, *Adv. Funct. Mater.*, 2008, **18**, 3941-3946.
71. T. D. Bogart, D. Oka, X. Lu, M. Gu, C. Wang and B. A. Korgel, *ACS Nano*, 2013, **10.1021/nn405710w**.
72. F.-W. Yuan, H.-J. Yang and H.-Y. Tuan, *ACS Nano*, 2012, **6**, 9932-9942.
73. E. Kang, Y. S. Jung, A. S. Cavanagh, G.-H. Kim, S. M. George, A. C. Dillon, J. K. Kim and J. Lee, *Adv. Funct. Mater.*, 2011, **21**, 2430-2438.
74. N. Yan, L. Hu, Y. Li, Y. Wang, H. Zhong, X. Hu, X. Kong and Q. Chen, *J. Phys. Chem. C*, 2012, **116**, 7227-7235.
75. S. H. Lee, S.-H. Yu, J. E. Lee, A. Jin, D. J. Lee, N. Lee, H. Jo, K. Shin, T.-Y. Ahn, Y.-W. Kim, H. Choe, Y.-E. Sung and T. Hyeon, *Nano Lett.*, 2013, **13**, 4249-4256.
76. B. Jang, M. Park, O. B. Chae, S. Park, Y. Kim, S. M. Oh, Y. Piao and T. Hyeon, *J. Am. Chem. Soc.*, 2012, **134**, 15010-15015.